Drop motion induced by vertical vibrations

New Journal of Physics
The open access journal at the forefront of physics

Deutsche Physikalische Gesellschaft DPG IOP Institute of Physics

PAPER • OPEN ACCESS

Drop motion induced by vertical vibrations

To cite this article: Paolo Sartori *et al* 2015 *New J. Phys.* **17** 113017

New Journal of Physics
The open access journal at the forefront of physics

Deutsche Physikalische Gesellschaft DPG
IOP Institute of Physics

Published in partnership with: Deutsche Physikalische Gesellschaft and the Institute of Physics

OPEN ACCESS

RECEIVED
5 August 2015

ACCEPTED FOR PUBLICATION
24 September 2015

PUBLISHED
3 November 2015

PAPER

Drop motion induced by vertical vibrations

Paolo Sartori[1], **Damiano Quagliati**[1], **Silvia Varagnolo**[1], **Matteo Pierno**[1], **Giampaolo Mistura**[1,3], **Francesco Magaletti**[2] **and Carlo Massimo Casciola**[2]

[1] CNISM and Dipartimento di Fisica e Astronomia G.Galilei, Università di Padova, via Marzolo 8, I-35131 Padova, Italy
[2] Dipartimento di Ingegneria Meccanica e Aerospaziale, Università La Sapienza, Via Eudossiana 18, I-00184 Roma, Italy
[3] Author to whom any correspondence should be addressed.

E-mail: giampaolo.mistura@unipd.it **and** carlomassimo.casciola@uniroma1.it

Keywords: moving drops, drop actuation, vertical vibrations

Supplementary material for this article is available online

Abstract

We have studied the motion of liquid drops on an inclined plate subject to vertical vibrations. The liquids comprised distilled water and different aqueous solutions of glycerol, ethanol and isopropanol spanning the range 1–39 $mm^2\ s^{-1}$ in kinematic viscosities and 40–72 $mN\ m^{-1}$ in surface tension. At sufficiently low oscillating amplitudes, the drops are always pinned to the surface. Vibrating the plate above a certain amplitude yields sliding of the drop. Further increasing the oscillating amplitude drives the drop upward against gravity. In the case of the most hydrophilic aqueous solutions, this motion is not observed and the drop only slides downward. Images taken with a fast camera show that the drop profile evolves in a different way during sliding and climbing. In particular, the climbing drop experiences a much bigger variation in its profile during an oscillating period. Complementary numerical simulations of 2D drops based on a diffuse interface approach confirm the experimental findings. The overall qualitative behavior is reproduced suggesting that the contact line pinning due to contact angle hysteresis is not necessary to explain the drop climbing.

1. Introduction

A drop deposited on a substrate, tilted with respect to the horizontal by a sufficiently small angle, does not move. Inclining the substrate above a certain characteristic angle induces downward sliding of the drop because of gravity. On a flat, homogenous surface sliding occurs at a characteristic constant speed U, which increases with the inclination angle. Such a motion is the result of a balance between the down-plane component of the drop weight and the viscous resistance, plus a capillary force related to the nonuniformity of the contact angle along the drop perimeter [1, 2]. Patterning the surface with parallel lyophilic and lyophobic stripes causes a stick-slip motion whose average speed is an order of magnitude smaller than that measured on a homogeneous surface having the same static contact angle [3]. More generally, experiments on chemically heterogeneous surfaces formed by domains of various shapes printed on substrates having different wettability and arranged in diverse symmetric patterns [4–6] show that the chemical pattern of a surface can passively tune the sliding behavior of drops. A surface having a spatial gradient of hydrophobicity is also capable of causing drops of water placed on it to move upward [7]. Recently, upward motion of drops on inclined heterogeneous substrates has also been theoretically analized [8].

For polar liquids, electrowetting provides an active way to control drop motion on a solid surface [9]. Fluid manipulations at the microscale and beyond are powerfully enabled through the use of ultrasonic surface acoustic waves [10]. A more exotic drop actuation relies on the so-called Leidenfrost phenomenon, that is the levitation of drops on a cushion of vapor produced when they are brought in contact with a hot solid [11]. Vibrations of the substrate are also used as an active way to control drop motion of any liquid because they couple to the liquid inertia. For instance, drops on a horizontal plate vibrating tangentially can depin from surface defects and move [12]. If the plate vibrates parallel to gravity, the contact line oscillations are rectified by hysteresis, thus inducing a ratcheting motion to the water drop vertically downward [13]. Interestingly, Brunet

et al [14, 15] found that drops on an inclined plane subject to sufficiently strong vertical vibrations can climb against gravity. An extension of this study shows that drops can be moved on a flat surface by simultaneous vertical and horizontal vibrations that are phase-shifted [16].

The surprising drop climbing was originally explained as a breaking of the front–back symmetry of the oscillating drop and a nonlinear friction law between the drop and the plane [14]. This phenomenon was also studied theoretically assuming thin, two-dimensional drops. John and Thiele [17] examined the limit of low Reynolds numbers and modeled the drop's contact line by precursor films due to van der Waals forces. They found that the component of the vibration orthogonal to the plate induces a nonlinear response in the drop shape that causes an anharmonic response of the drop to the parallel vibration component. Benilov and Billingham [18] analyzed the opposite limit of low viscosity and observed that the climbing motion is due to an interaction of oscillatory modes induced by vibrations. These studies were then extended to a first 3D modeling of climbing drops on oscillating substrates under the assumptions of weak vibrations, low viscosity and inertia of the liquid, thin drops and contact-line law [19]. The main conclusion was that, at low frequency, the 2D model [18] is qualitatively incorrect because it predicts that 2D drops can climb only for a very large acceleration of the plate, whereas, for 3D drops, the acceleration can be finite.

To better clarify this intriguing phenomenon, we have systematically studied the dynamics of various water solutions covering an ample range of kinematic viscosities and dynamic contact angles. The measurements have been compared with the results of numerical simulations based on a diffuse interface approach. In particular we chose the Cahn–Hilliard/Navier–Stokes (CHNS) model because of its proven ability to handle the contact line dynamics [20, 21]. It is also embedded with capillary stresses all along the droplet interface and handles extreme interface deformations, up to the droplet breakup [22]. Several other approaches have been exploited to study flows with contact line motion [23]. Recently Kim *et al* [24] applied a lattice Boltzmann method (LBM) to study the dynamics of a droplet on a moving wall, analyzing the effect of the wettability on the onset of the droplet pinch off. The motion onset of a drop on a homogenous plane, driven by a body force, was also investigated by Semprebon *et al* [25] by means of the Surface Evolver. Sbragaglia *et al* [26] instead applied a LBM to examine the sliding dynamics of a droplet on a heterogeneous patterned wall. A similar problem was investigated in [27] by means of the CHNS model. The volume of fluid method has also been applied to the sliding droplet problem and the influence of the contact angle hysteresis [28]. However, to the best of our knowledge, the motion of a droplet on a vibrating plate has not been studied using numerical methods which account for the fluid dynamics of the complete binary system. This is a challenging problem from the modeling and the computational points of view since the non-equilibrium contact angle dynamics plays a crucial role, especially in the high frequency range. After a description of the experimental and numerical methods used in this study, in section 3 we present and analyze the main results and discuss them in the conclusions.

2. Methods

2.1. Experimental setup

We have studied the dynamics of drops deposited on poly(methyl methacrylate) (PMMA) wedges with an inclination angle $\alpha = 30^\circ$ attached to the moving shaft of an electromagnetic shaker (LDS V101 Brüel & Kjær) as shown in the schematic diagram of figure 1. The shaker oscillates vertically in the frequency range 10 Hz $-$10 KHz with a maximum amplitude of 2.5 mm and the maximum force it can exert is 8.9 N. In order to constrain the drop motion to one-dimension, we have sculpted channels of different cross-sections (circular, triangular and rectangular) and different widths (from about 0.2 to 4 mm) along the direction of the tangential component of the acceleration of gravity. The one we found most effective is a square ridge having height of 2 mm and width of 3 mm (see figure 1). Its vertical extension allowed us to more easily focus the side-view camera to the drop illuminated by the backlight LED source.

To find the most appropriate drop volume, we have systematically investigated the reproducibility of the drop dynamics. Water drops of increasing volume are deposited with a syringe pump (UltraMicroPump UMP3, WPI) at the center of the ridge. The drops are initially pinned to the surface. Vertical oscillations of the substrate above a given acceleration a_{sliding} cause a downward sliding of the drop. The graph of figure 1 shows the dispersion of the acceleration threshold for sliding $\Delta a_{\text{sliding}}$ measured as a function of the drop volume for a ridge with a width of 3 mm and an oscillating frequency of 80 Hz. The dispersion $\Delta a_{\text{sliding}}$ is the root mean square deviation calculated from a statistical ensemble of at least five data points acquired at the same nominal conditions. The graph shows a sudden increase in $\Delta a_{\text{sliding}}$ just above 2.5 μL. We explain it as due to the interaction of the drop contact line with the lateral, irregular edges of the ridge. Actually, the inset compares the expected diameter d_C of a hemispherical sessile drop of volume V with the measured longitudinal d_L and transversal d_W elongations of the contact line. At small volumes, these three quantities coincide confirming that the contact line is circular. Above 2.5 μL, d_W lies below d_C confirming that one side of the contact touches the

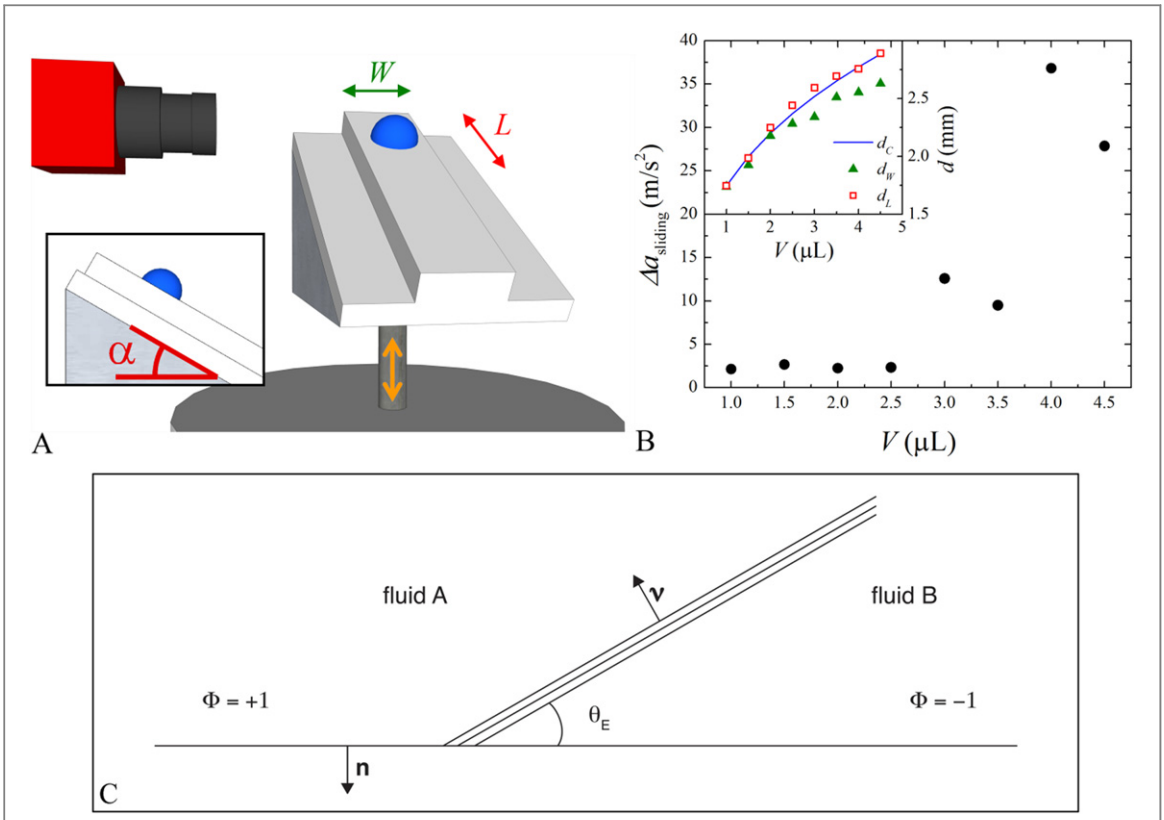

Figure 1. (A) Schematic drawing of the experimental set-up. (B) Dispersion of the acceleration threshold for sliding $\Delta a_{sliding}$ as a function of the drop volume for a ridge with a width of 3 mm oscillating at a frequency of 80 Hz. Inset: comparison of the expected diameter d_C of a hemispherical sessile drop of volume with the measured longitudinal d_L and transversal d_W elongations of the contact line. (C) Sketch of the contact line region where the interface between the two fluids forms an angle θ_E with the tangent to the substrate. Here $\boldsymbol{\nu}$ and $\mathbf{n}$ are the normal to the interface and the outward normal to the substrate, respectively.

edge. The fact that d_L remains equal to d_C means that the lateral contact angle is increased because of the geometric pinning at the edge [29].

In our study we have then used drops of 2 μL because they can be easily and accurately detected with our optical set-up. Furthermore, the lateral extension of the ridge guarantees that during their motion the lateral displacement amounts to no more than 0.4 mm, otherwise they will pin to or fall down the edges. In this way, we can accurately track the (one-dimensional) motion of drops by using only one video camera. We have also compared the sliding of 2 μL water drops on the ridge with that on a flat surface and could not detect any appreciable difference between the two substrates.

Besides distilled water, we have also studied different aqueous solutions of glycerol, ethanol and isopropanol. In addition, we have modified the wettability of the PMMA by coating it with trichloro(1H,1H,2H,2H-perfluorooctyl)silane. Their main physical parameters are listed in table 1. The values of density ρ, viscosity μ and surface tension σ refer to a temperature of 25 °C and have been deduced from literature [30, 31]. The addition of ethanol and isopropanol mainly decreases the surface tension of the mixture, while that of glycerol increases the viscosity. The kinematic viscosities ν of these mixtures cover the range 1–39 mm^2 s^{-1}, much wider than the interval between 31 and 55 mm^2 s^{-1} of the glycerol–water mixtures originally studied by Brunet *et al* [14]. The equilibrium contact angle θ_E and the advancing (receding) contact angle θ_A (θ_R) are determined using the optical apparatus described in [29]. In particular, θ_A and θ_R are measured, respectively, by inflating and deflating a drop deposited on the horizontal surface with the syringe pump and observing the profile when the contact line starts moving. This study is completed with the determination of the contact angle hysteresis $\Delta\theta = \theta_A - \theta_R$, which quantifies the surface pinning. All these data are listed in table 1. We have also measured the surface roughness of the top face of the PMMA ridge with a profilemeter and got an rms value less than a couple of nm.

2.2. Numerical method

The numerical simulations are based on a diffuse interface approach, the CHNS model, to deal with the flow of two immiscible fluids where capillary effects and contact line motion play a crucial role on the fluid dynamics.

Table 1. Main physical parameters of the different aqueous solutions used in this study. The wettability properties are characterized by the equilibrium contact angle θ_E, the advancing contact angle θ_A and the receding contact angle θ_R.

Fluid solution	ρ (g cm^{-3})	μ (mPa s)	σ (mN m^{-1})	θ_E	θ_A	θ_R	$\Delta\theta$	Substrate
Water	0.997	0.89	72	71° ± 2°	87° ± 2°	66° ± 3°	21° ± 5°	PMMA
9% (w/w) of ethanol in water	0.98	1.35	52.4	63° ± 3°	79° ± 3°	62° ± 3°	17° ± 6°	PMMA
17% (w/w) of ethanol in water	0.97	1.83	48.8	57° ± 3°	72° ± 1°	50° ± 3°	22° ± 4°	PMMA
5% (w/w) of isopropanol in water	0.988	1.12	49.6	64° ± 3°	75° ± 3°	53° ± 3°	22° ± 5°	PMMA
10% (w/w) of isopropanol in water	0.981	1.41	40.4	61° ± 2°	71° ± 3°	54° ± 3°	17° ± 5°	PMMA
60% (w/w) of glycerol in water	1.15	9	67.2	69° ± 1°	78° ± 1°	67° ± 3°	11° ± 4°	PMMA
80% (w/w) of glycerol in water	1.2	47	65	70° ± 1°	79° ± 2°	67° ± 2°	12° ± 4°	PMMA
Water	0.997	0.89	72	115° ± 2°	118° ± 2°	69° ± 2°	49° ± 4°	Silanized PMMA

We here briefly introduce the mathematical model with particular attention to the boundary conditions and we refer to [6, 21, 26, 32, 33] for a detailed derivation and some applications.

The binary system constituted by two pure, immiscible fluids of density ρ_A and ρ_B, respectively, is described by a scalar function, the *phase field* $\Phi(\boldsymbol{x},\ t)$, defined as $\Phi(\boldsymbol{x},\ t) = 2[\rho(\boldsymbol{x},\ t) - (\rho_A + \rho_B)/2]/(\rho_A - \rho_B)$, where $\rho(\boldsymbol{x},\ t)$ is the local density of the mixture, such that $-1 \leqslant \Phi \leqslant 1$. The Cahn–Hilliard model corresponds to a non-local free energy functional

$$F[\Phi] = \int_\Omega \left(f_{\text{bulk}}(\Phi) + \frac{\lambda}{2} |\nabla\Phi|^2 \right) \mathrm{d}V + \int_{\partial\Omega} f_w(\Phi)\,\mathrm{d}S, \tag{1}$$

where $\lambda = 3\sigma\epsilon/\sqrt{8}$ is a coefficient related to the surface tension σ and to the interface thickness ϵ, combined with the constraint of mass conservation of the two species.

A common choice for the bulk free energy density is the double-well $f_{\text{bulk}} = \lambda(\Phi^2 - 1)^2/(4\varepsilon^2)$, which drives the system to the two equilibrium points $\Phi = \pm 1$, i.e. $\rho = \rho_A$ or $\rho = \rho_B$, respectively. Conversely, the gradient excess term $(\lambda/2)|\nabla\Phi|^2$ energetically penalizes the formation of sharp interfaces and accounts for surface tension. As a consequence of these two counteracting mechanisms, a finite thickness interface (width of order ε), across which Φ varies smoothly, separates the two bulk fluids in such a way to minimize the interfacial energy. The presence of the wall modifies this equilibrium, as prescribed by the last term $f_w(\Phi) = A\,\Phi(3 - \Phi^2)/4 + B$ that accounts for the fluid-wall interaction [21]. The wall energy f_w describes the wetting properties of the surface with respect to the two immiscible fluids, air and liquid in the drop, and the two coefficients A and B are identified by requiring that the solid-fluid surface energies, σ_{wA} and σ_{wB}, are recovered at the wall where $\Phi = \pm 1$, respectively, leading to $A = \sigma_{wA} - \sigma_{wB}$ and $B = (\sigma_{wA} + \sigma_{wB})/2$.

The model can be extended to unsteady isothermal conditions in presence of fluid motion described by the velocity field $\boldsymbol{u}$. Under the assumption of a small density variation, i.e. $2(\rho_A - \rho_B)/(\rho_A + \rho_B) \ll 1$, the velocity field is solenoidal to first order in the density variation, and the dimensionless form of the system reads

$$\nabla \cdot \boldsymbol{u} = 0, \tag{2}$$

$$\frac{\mathrm{D}\Phi}{\mathrm{D}t} = \frac{M}{\mathrm{Cn}} \nabla^2 \mu_c, \tag{3}$$

$$\frac{\mathrm{D}\boldsymbol{u}}{\mathrm{D}t} = -\nabla p + \frac{1}{\mathrm{We}\,\mathrm{Cn}} \mu_c \nabla\Phi + \frac{1}{\mathrm{Re}} \nabla^2 \boldsymbol{u} + \frac{1}{\mathrm{Fr}} \boldsymbol{g}. \tag{4}$$

In equations (3) and (4) $\mathrm{D}(\ \cdot\ )/\mathrm{D}t = \partial(\ \cdot\ )/\partial t + \boldsymbol{u} \cdot \nabla(\ \cdot\ )$ is the material derivative, $M = 3M^*\sigma/(\sqrt{8}L^3 f)$ is the dimensionless mobility coefficient where the mobility M^* is related to the time needed by the two fluids to reach an equilibrium state inside the interface and $\mathrm{Cn} = \epsilon/L$ is the Cahn number, i.e. the ratio of the interface thickness to the macroscopic length L. The chemical potential μ_c is defined as the functional derivative of the free energy (1) with respect to the phase field, $\mu_c = \delta F/\delta\Phi = \Phi^3 - \Phi - \mathrm{Cn}^2\,\nabla^2\Phi$. In equation (4), p is the dimensionless pressure, $\mathrm{Re} = \rho L^2 f/\mu$ is the Reynolds number with μ the viscosity and f the frequency of the vibrating plate, $\mathrm{We} = 3\rho f^2 L^3/(\sqrt{8}\,\sigma)$ is the Weber number, $\mathrm{Fr} = L\rho/(4\pi^2 A\Delta\rho)$ is the Froude number, with A the amplitude of the plate oscillation and $\Delta\rho = \rho_A - \rho_B$. In the reference frame of the plate inclined by the angle α, the vibration corresponds to a time dependent body force that gives rise to a buoyancy term. Assuming the peak acceleration of the vibrating plate much larger than the gravitational one, we can neglect the latter constant contribution. From the definition of Φ, the density is expressed as $\rho(\Phi) = \rho_M + \Delta\rho\Phi/2$ where $\rho_M = (\rho_A + \rho_B)/2$ and $\Delta\rho = \rho_A - \rho_B$. For the sake of simplicity, we assume $\Delta\rho/\rho_M \ll 1$, so that, in the spirit of Boussinesq approximation, the only effect of buoyancy is retained in the body force $\boldsymbol{g}(t) = -\sin(2\pi t)(\sin\alpha\hat{\mathbf{e}}_x + \cos\alpha\hat{\mathbf{e}}_z)\Phi/2$ with $\hat{\mathbf{e}}_{x,z}$ the unit vectors along the two main directions, parallel and perpendicular to the plate. At variance with the standard application of the Boussinesq approximation, where the driving force is the temperature difference that leads to density variations via thermal expansion of the fluid, here the driving force is the phase field difference associated to the density contrast $\Delta\rho$.

Under normal conditions, the physical interface thickness is on the nanometer scale and the model cannot be exploited for macroscopic flows unless an artificial thickening of the interface is introduced. It is crucial that such artificial thickening does not alter the dynamics. Indeed the *sharp interface limit* is obtained when the macroscopic solution becomes independent of Cn and M as they decrease their values. In [33] the scaling law $M \propto \mathrm{Cn}^2$ is shown to be crucial in approaching the physically meaningful solution in the limit of decreasing Cahn number, which is recovered at $\mathrm{Cn} = \mathcal{O}(10^{-2})$.

The system of equations is completed with the following boundary conditions:

$$\boldsymbol{u} = 0, \tag{5}$$

$$\nabla\mu_c \cdot \boldsymbol{n} = 0 \tag{6}$$

implying the no-slip and no mass flux conditions at the wall, respectively, and

$$\frac{\mathrm{D}\Phi}{\mathrm{D}t} = -\frac{\mathrm{Re}}{D_w\,\mathrm{We}\,\mathrm{Cn}}\left(\Phi^2 - 1\right)\cos\theta_E - \frac{\mathrm{Re}}{D_w\,\mathrm{We}}\frac{\partial\Phi}{\partial n}, \tag{7}$$

where $D_w = \mu_f/\mu$, with μ_f an effective friction of the contact line, represents the ratio of the typical relaxation time in reaching the equilibrium contact angle to the macroscopic time scale [32].

In contrast to the first two boundary conditions, whose interpretation is straightforward, equation (7) needs some comments. Let us consider the equilibrium conditions first, where the derivative on the left-hand side of (7) vanishes. The equilibrium condition is characterized by the minimum of the free energy functional, equation (1). The Euler–Lagrange equations consist of a bulk term that leads to $\mu_c = \text{const}$ and a boundary term that reads

$$\frac{\partial f_w}{\partial\Phi} + \lambda\frac{\partial\Phi}{\partial n} = \frac{3}{4}(\sigma_A - \sigma_B)\left(1 - \Phi^2\right) + \frac{3}{\sqrt{8}}\sigma\varepsilon\frac{\partial\Phi}{\partial n} = 0, \tag{8}$$

i.e. $(\sigma_A - \sigma_B)(1 - \Phi^2) = -\sqrt{2}\,\varepsilon\sigma\partial\Phi/\partial n$. In the part of the boundary in contact with a pure fluid, either fluid A ($\Phi = +1$) or fluid B ($\Phi = -1$), the equation reduces to $\partial\Phi/\partial n = 0$. Let us now consider the narrow part of the boundary where the interface of width ε between the two pure phases meets the boundary and denote by θ_E the angle formed by the $\Phi = 0$ isoline and the boundary, see the sketch reported in figure 1. Since the same angle is formed by the normal $\boldsymbol{\nu}$ to the interface and the normal $-\boldsymbol{n}$ to the boundary (the sign comes from the definition of $\boldsymbol{n}$ as unit outward normal), $-\boldsymbol{n}\cdot\boldsymbol{\nu} = \cos\theta_E$. Along the interface between the two pure fluids, the gradient of the phase field is normal to the interface itself, i.e. $\nabla\Phi = \boldsymbol{\nu}\partial\Phi/\partial\nu$. There results the identity $\partial\Phi/\partial n = \boldsymbol{n}\cdot\nabla\Phi = -\partial\Phi/\partial\nu\,\cos\theta_E$, which substituted in the steady state boundary condition (8) when $\Phi = 0$ yields $(\sigma_A - \sigma_B) = \sqrt{2}\,\varepsilon\sigma\,\cos(\theta_E)\,\partial\Phi/\partial n\,|_{\Phi=0}$. Considering now the expression for the phase field across an equilibrium interface (see [21, 33] for details), $\Phi = \tanh(\nu/(\sqrt{2}\,\varepsilon))$, we obtain $\partial\Phi/\partial n\,|_{\Phi=0} = 1/(\sqrt{2}\,\varepsilon)$. Hence we arrive at $(\sigma_A - \sigma_B) = \sigma\cos(\theta_E)$, which expresses the angle θ_E in terms of the surface and interfacial energy densities. This result allows to identify θ_E as the classical Young contact angle. We point out that the reasoning qualitatively illustrated above is more properly understood in the limit as the interface thickness vanishes.

The system of equations has been discretized by finite differences on a staggered and uniform grid using central second-order approximations. The time integration is performed with a semi-implicit scheme where the linear part is treated implicitly by means of a classical Crank–Nicolson second-order approximation, while a four-stage, third order, low-storage Runge–Kutta is used for the nonlinear part. The incompressible Navier–Stokes equation has been solved with a classical projection method. More details about the numerical scheme used can be found in [33]. In order to work in the asymptotic sharp interface regime, $\mathrm{Cn} = 0.025$ and $M = \mathrm{Cn}^2 = 6.25\times10^{-4}$ have been used throughout the simulations. The equilibrium contact angle has been chosen slightly hydrophobic, $\theta_E = 97.5°$ and, following [32], we selected $D_w = 100$. For density, viscosity and surface tension we used the typical values for water reported in table 1. We considered a 1 mm radius drop and, in order to compare the numerical results with the experiments, we used $\Delta\rho/\rho = 1$ relying on the ability of the Boussinesq approximation to qualitatively reproduce the correct physics.

3. Results and analysis

The motion of the drop is found to depend on the acceleration a and on the frequency f of the vertical vibrations. Figure 2 displays the dynamical phase diagrams of the five aqueous solutions obtained by scanning, at different constant frequencies, the vertical acceleration. To better compare them, the oscillating frequency is normalized [14] to the resonance frequency of the drop's rocking mode corresponding to a supported drop vibrated in a direction parallel to the substrate [34]:

$$f_0 = \frac{1}{2\pi R^{3/2}}\sqrt{\frac{6\sigma h\left(\theta_E\right)}{\rho\left(1 - \cos\theta_E\right)\left(2 + \cos\theta_E\right)}}, \tag{9}$$

where R is the radius of the truncated spherical drop of volume V and $h(\theta_E)$ is a dimensionless geometric function of the equilibrium contact angle θ_E. For droplets on PMMA, θ_E is always less than 90° and then $h = 1$, while for water droplets on silanized PMMA $h(\theta_E = 115°) = 0.4$. The radius R can be calculated from [29]

$$R^3 = \frac{3V}{\pi}\frac{1}{\left(1 - \cos\theta_E\right)^2\left(2 + \cos\theta_E\right)}. \tag{10}$$

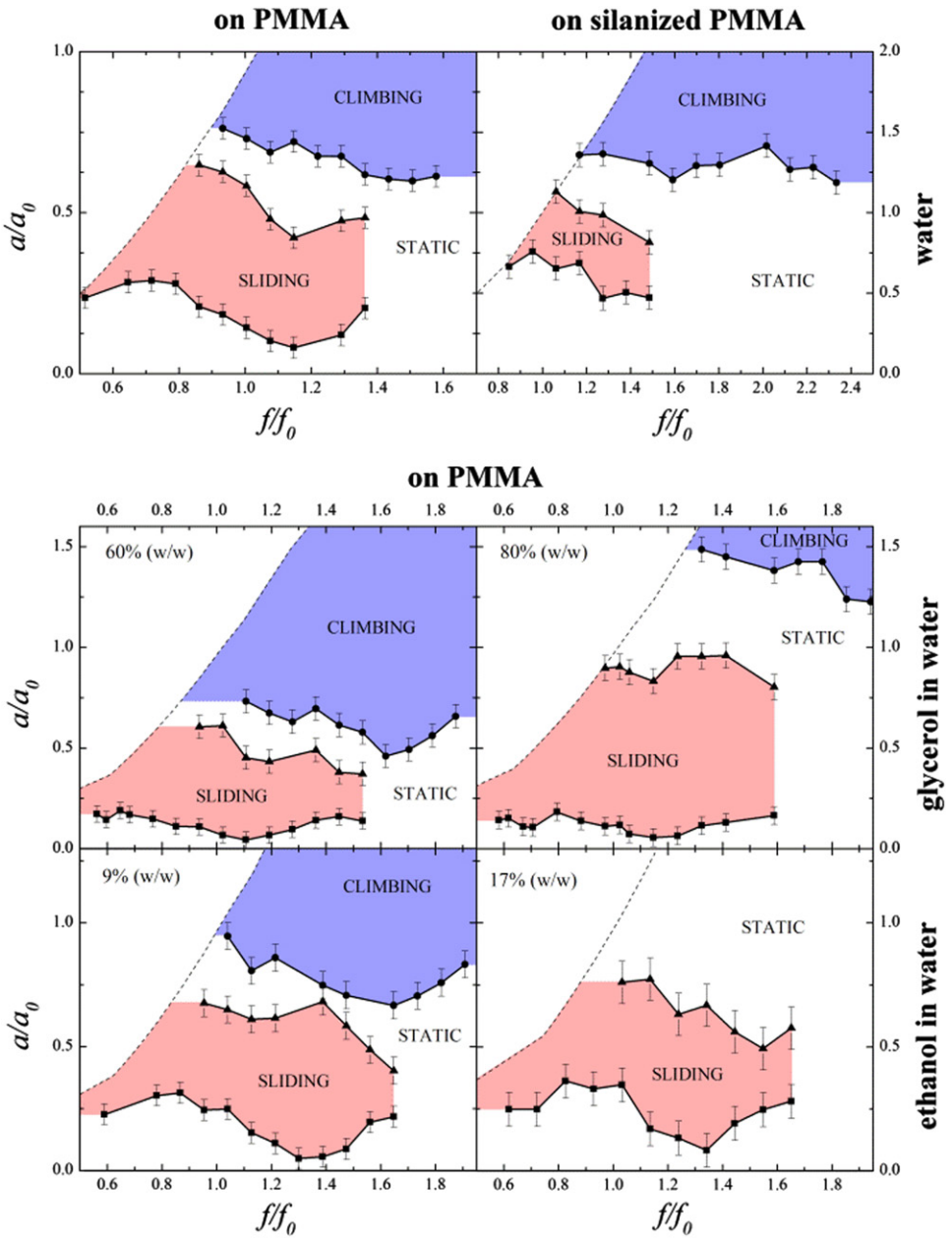

Figure 2. Dynamical phase diagrams of drops of different aqueous solutions corresponding to $V = 2\ \mu L$ and $\alpha = 30°$. The normalization factors are $a_0 = 241\ \text{m s}^{-2}$ and $f_0 = 70$ Hz for water on PMMA and $a_0 = 110\ \text{m s}^{-2}$ and $f_0 = 47$ Hz for water on silanized PMMA. For the other liquids they are comprised in the ranges $a_0 = 117$–$173\ \text{m s}^{-2}$ and $f_0 = 48-59$ Hz.

The acceleration is determined from the formula:

$$a = 4\pi^2 f^2 A, \tag{11}$$

where A is the oscillating amplitude, which is deduced from the maximum displacement of the ridge measured with the high frequency camera. The characteristic acceleration is taken as

$$a_0 = 4\pi^2 f_0^2 V^{1/3}, \tag{12}$$

since $V^{1/3}$ is a measure of the deformation [14]. For 2 μL water drops on PMMA, the two characteristic parameters are $f_0 = 70$ Hz and $a_0 = 241\ \text{m s}^{-2}$, while on silanized PMMA $f_0 = 47$ Hz and $a_0 = 110\ \text{m s}^{-2}$. For the other liquids on PMMA these values become smaller and are comprised in the ranges $f_0 = 34$–59 Hz and $a_0 = 59$–$173\ \text{m s}^{-2}$.

The phase diagrams of glycerol/water mixtures look quite similar to that originally reported for a drop of water-glycerol having $V = 5\ \mu$L and $\nu = 31\ \text{mm}^2\ \text{s}^{-1}$ deposited on an inclined plane with $\alpha = 45°$ [14] (the parabolic dashed lines in the diagrams of figure 2 represent the relative acceleration corresponding to the maximum oscillating amplitude of our shaker equal to 2.5 mm). On the static ridge, the drops are always pinned

to the surface. Vertically vibrating the ridge above a certain relative acceleration $a/a_0 \sim 0.2$, very similar to that found by Brunet *el al* [14], yields sliding of the drop. Furthermore, sliding can be induced only for relative frequencies f/f_0 smaller than ~1.5, which is close to the cut-off of ~1.3 reported for a 5 μL glycerol/water drop for $\alpha = 45°$ [14]. At variance with previous experiments that could not detect sliding for drops of volume smaller than 5 μL [14, 15], we always observed a sliding region for all the 2 μL drops we investigated, an indication that our surfaces were not too defective. Also, no evidence of drop breaking was found during our measurements in contrast to what reported by Brunet *et al* [14, 15], probably because of the smaller drops we used.

We now discuss in more detail the single phase diagrams, starting from that of pure water on PMMA that presents a pronounced sliding region at moderate accelerations: for $f/f_0 = 0.9$ and $a/a_0 = 0.4$ the sliding velocity is about 6.4 mm s^{-1}. Further increasing the oscillating amplitude moves the drop upwards against gravity: for $f/f_0 = 1.1$ and $a/a_0 = 1.1$ the climbing velocity is 4.3 mm s^{-1}. As expected, the overall phase diagram closely resembles those of mixtures of 9% (w/w) of ethanol in water and 5% (w/w) of isopropanol in water (not shown because it has fewer points) because these solutions have essentially the same viscosity and similar wetting properties of pure water. More interesting, it is also very similar to those of glycerol/water mixtures in spite of a variation in ν greater than a factor 10. This finding is consistent with the observation that the threshold for climbing with liquids of similar surface tensions does not depend on the liquid viscosity [15]. If instead we compare it with that of water on silanized PMMA, we notice that the sliding and climbing regions have been shifted to higher relative accelerations to balance the higher capillarity forces due to contact-angle hysteresis that, on silanized PMMA, is more than twice the value measured on PMMA, as reported in table 1. Arguably, the most interesting and original result of our experimental study is that drops of 17% (w/w) of ethanol in water and of 10% (w/w) of isopropanol in water do not climb within the a/a_0 range accessible to the experiment clearly indicating that a wettable ridge favors sliding only. This is somewhat unexpected because the properties of these solutions differ slightly from those of the 9% (w/w) ethanol/water and 5% (w/w) isopropanol/water mixtures. More systematic measurements involving solution at different concentrations are required to better characterize the sudden disappearance of the climbing phase.

With a fast camera we have analyzed the drop evolution during sliding and climbing. Figure 3 shows a sequence of side view snapshots taken over an oscillating period (see also Movie1 and Movie2 in supplemental material). They clearly show that the instantaneous drop profile varies differently in the two situations. The evolution of the climbing drop experiences a bigger variation in the profile: the peak becomes sharper (see *E–D*) and the bump is wider and shallower (see *F–G*).

From the analysis of these images, we have extracted the evolution of the upper and lower instantaneous contact angles, θ_{up} and θ_{down} respectively, which are shown in figure 4 for the two cases just discussed. In the same graphs, the corresponding positions of the contact points are also plotted. All quantities oscillate periodically over time. In particular, the positions display an oscillatory behavior around a mean value that slowly moves downward (upward) when the drop slides (climbs). It is clearly evident that the lower (upper) contact point of a sliding drop moves downward when the corresponding contact angle is above (below) the advancing (receding) contact angle, as shown by the shaded areas in figure 4. Similarly, the upper (lower) contact point of a climbing drop moves upward when the corresponding contact angle is above (below) the advancing (receding) contact angle.

Furthermore, the contact angles, as well as the contact line positions, are out of phase with the oscillation of the inclined plate. The phase shift δ_{down} (δ_{up}) between the lower (upper) contact point velocity and the lower (upper) contact angle for sliding and climbing drops driven at different frequencies are reported in figure 5. It results that the upper contact point velocity is always in phase with respect to the upper contact angle, while the lower contact point velocity is out of phase with the lower contact angle.

Before addressing the simulations of a drop sitting on the vibrating plate, we discuss preliminary results concerning a drop sliding down an inclined wall in order to determine the dependence of upper and lower contact angles on the sliding velocity. The results are plotted in the graph of figure 6 as a function of the capillary number $Ca = \mu u/\sigma$ based on the sliding velocity U, considered positive at the advancing triple point ($u = |U|$) and negative at the receding triple point ($u = -|U|$), and refer to a slightly hydrophobic surface ($\theta_E \equiv \theta_D(Ca = 0) = 97.5°$). By changing the inclination angle from 0° to 30°, it is possible to explore the range 0–0.004 in Ca number. In each simulation, both θ_{down} and θ_{up} have been determined together with the sliding velocity. By definition, each sliding velocity provides two opposite Ca numbers, one positive corresponding to the lower contact line and one negative corresponding to the upper contact line. Hence, in the graph, the measured $\theta_D = \theta_{down}$ is related to the positive Ca, while the measured $\theta_D = \theta_{up}$ to the negative Ca branch. In the whole range of analyzed velocity we found an almost linear dependence of the contact angle on the capillary number which does not match with the $\theta_D \propto Ca^{1/3}$ scaling law obtained within the lubrication approximation [35]. We ascribe this dependence to the choice of constant D_w (in our simulations $D_w = 100$). A more accurate reproduction of the theoretical results could be obtained by suitably tuning D_w, but this is beyond the scope of

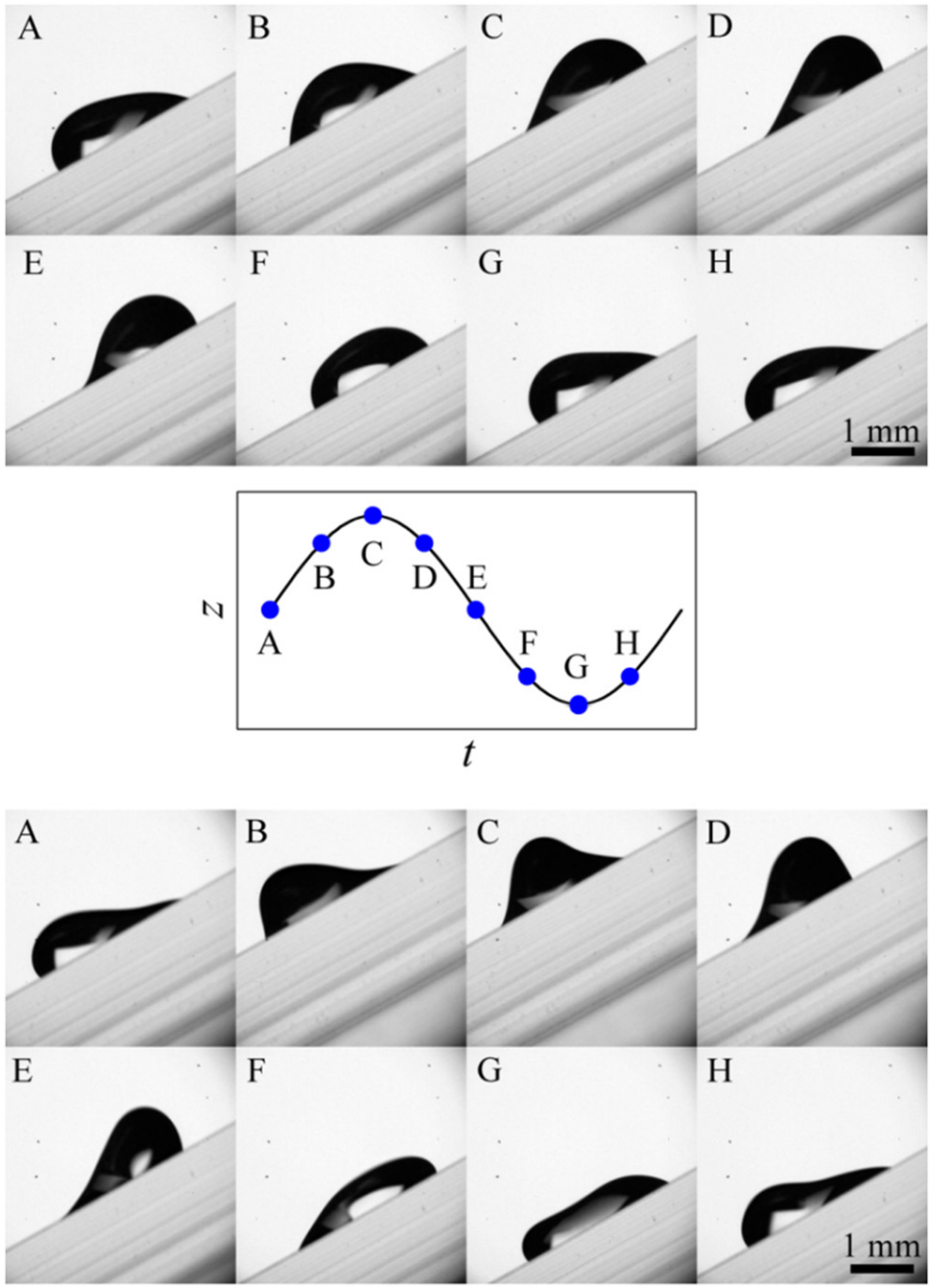

Figure 3. Side views of a sliding (top) and climbing (bottom) water drop taken at different instants of a vibrating cycle of frequency $f = 65$ Hz, e.g. $f/f_0 = 0.9$ for sliding ($f = 80$ Hz, e.g. $f/f_0 = 1.1$ for climbing) as indicated in the middle panel. The vertical accelerations are $a = 100$ m s^{-2} ($a/a_0 = 0.4$) for the sliding drop and $a = 260$ m s^{-2} ($a/a_0 = 1.1$) for the climbing drop.

this work. It is worthwhile to point out that the lubrication approximation is not valid in the case of hydrophobic surfaces since the drop shape is not thin. Moreover, experimental data [36] show an almost linear dependence of the dynamic contact angle on the Ca number. The capillary force has instead a nonlinear dependence on the contact line velocity, since $F_{\mathrm{cap}} \propto \sigma(\cos(\theta_D) - \cos(\theta_E))$. As suggested in [35] and as we will see later, this nonlinearity is crucial for the drop dynamics on the vibrating plate.

Extensive numerical simulations have been performed by changing the frequency and the amplitude of the vibrating plate. Before discussing the results, we point out that several significant differences exist between the systems we have numerically simulated and the corresponding experiments: (i) the simulations are two dimensional; (ii) the two fluids (corresponding to droplet liquid and surrounding air, in the experiment) have the same viscosity and almost identical densities. More precisely, the Boussinesq approximation is adopted, which implies that the density is constant apart from the buoyancy term; (iii) no pinning of the contact lines is considered; (iv) the plate is hydrophobic ($\theta_E = 97.5°$). Clearly, assumptions (i) and (ii) have been introduced for

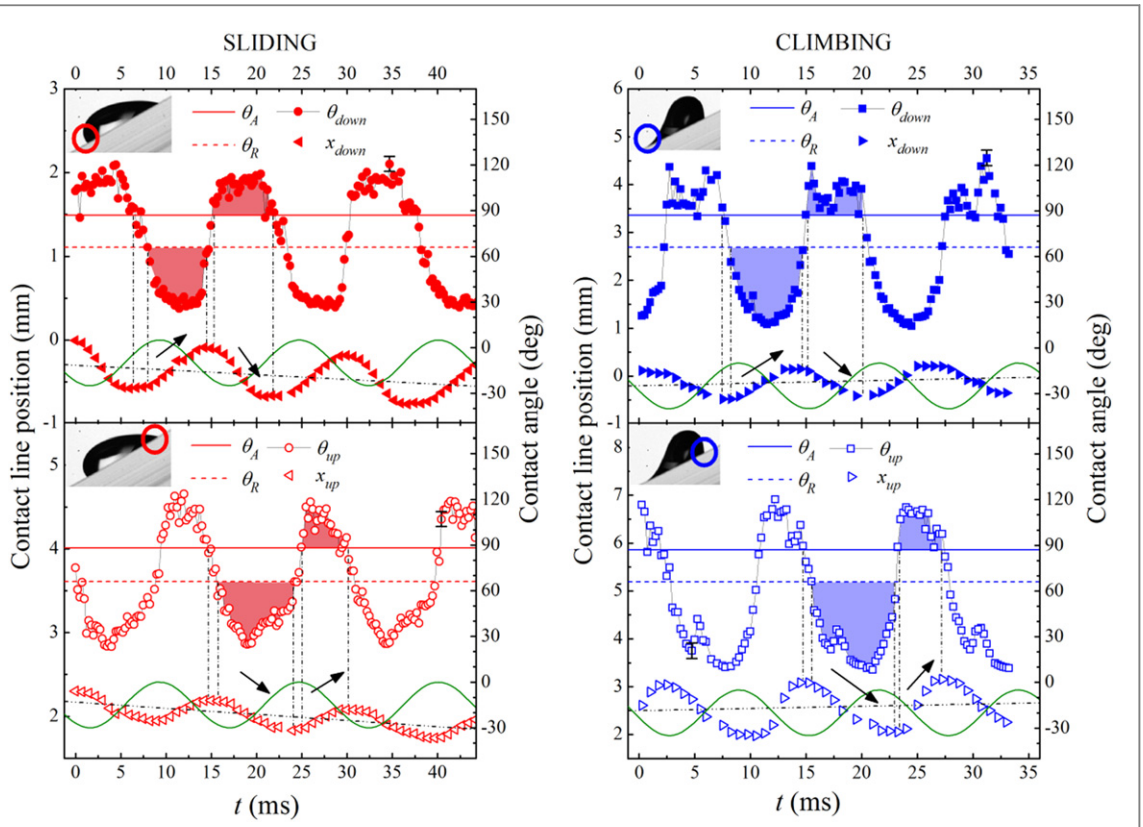

Figure 4. Time evolution of the upper and lower contact angles for a water drop sliding down (left panels) and climbing up (right panels) the inclined ridge. The corresponding contact line positions along the x direction of the inclined ridge are also plotted. Frequency and acceleration are $f = 65$ Hz and $a = 100$ m s^{-2} for the sliding drop and $f = 80$ Hz and $a = 260$ m s^{-2} for the climbing drop, respectively. The advancing (receding) contact angle is indicated by a continuous (dashed) horizontal line. The continuous sinusoidal lines represent the oscillation of the vertical position z of the inclined plate (in arbitrary units). The error on the contact angle is about 5°. For the sake of clarity , the corresponding error bars are reported only in one point for each contact angle. Instead, the error bars on the position are smaller than the symbols.

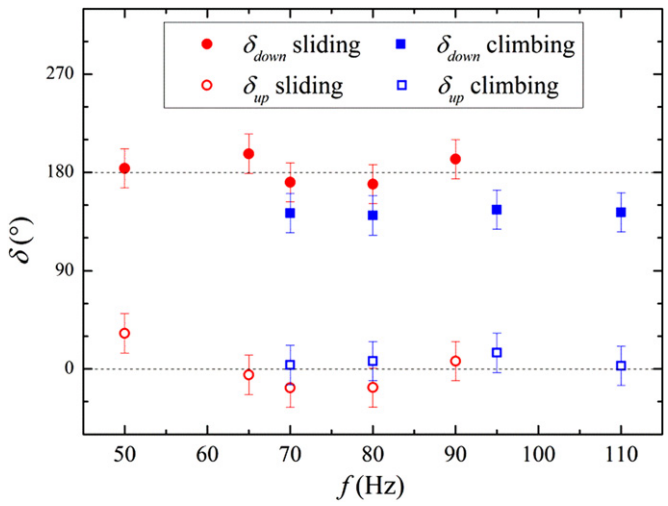

Figure 5. Phase shift $\delta_{\rm down}$ ($\delta_{\rm up}$) between the lower (upper) contact point velocity and the lower (upper) contact angle for the sliding drop and the climbing drop. In the sliding case the peak acceleration is fixed at $a = 80$ m s^{-2}, while in the climbing one it is fixed at $a = 200$ m s^{-2}.

simplicity. Assumption (iii) is due to the lack of reliable models for pinning in the context of diffuse interface models. Finally, drop climbing has been found only by assuming (iv). We cannot exclude that a more complete search could identify climbing also on slightly hydrophilic surfaces.

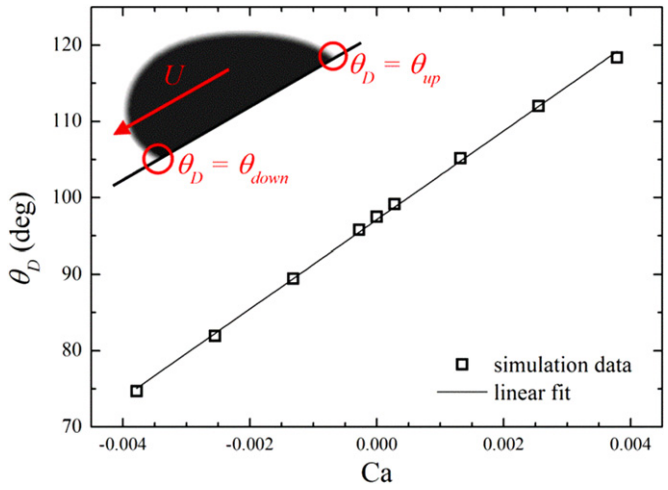

Figure 6. Lower and upper contact angles as a function of the capillary number Ca. The branch Ca > 0 (Ca < 0) refers to the lower (upper) contact angle, so that $\theta_D = \theta_{\rm down}$ ($\theta_D = \theta_{\rm up}$). The point Ca $= 0$ represents the static condition $\theta_D = \theta_E = 97.5°$ in our simulations.

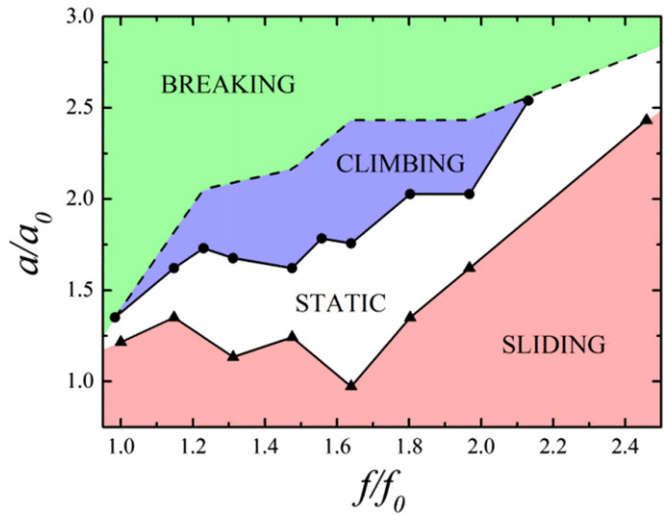

Figure 7. Dynamical phase diagram of water obtained by numerical simulations. The data correspond to $\alpha = 30°$ and $\theta_E = 97.5°$. The normalization factors are $a_0 = 185$ m s^{-2} and $f_0 = 61$ Hz.

Despite these differences, the dynamical phase diagram in figure 7 reproduces the main features observed in the experiments. At high acceleration the drop climbs. Reducing the oscillating amplitude at fixed frequency, a *non-pinned* static droplet is found. Because of the lack of pinning in the model, in this region the droplet periodically moves up and down without a mean displacement. Further decreasing a/a_0, the drop starts sliding. The numerical simulations cannot reproduce the static region found in the experiments at very low accelerations again because of the lack of pinning in the model. At very high accelerations, the drop detaches from the plane or, in some cases, breaks-up due to the extreme deformations. In the phase diagram in figure 7 the dashed curve identifies this breaking region. This sequence of dynamic transitions is found for all frequencies below a threshold value $\simeq 2f_0$, beyond which climbing disappears because the drop dynamics at high a/a_0 is dominated by detachment and break-up. This behavior, not observed in our experiments, is likely due to the 2D nature of the drops since the reduced capillary stress (in 2D simulations the second main curvature is zero) leads to greater elongations that facilitate the drop break-up. Similarly, the numerical transitions are found at higher relative accelerations than the experimental ones. Notwithstanding these discrepancies, the overall qualitative behavior is reproduced which means that neither the contact line pinning due to contact angle hysteresis, nor the density difference between the droplet and the ambient fluid, seems to be of crucial importance to describe the climbing mechanism.

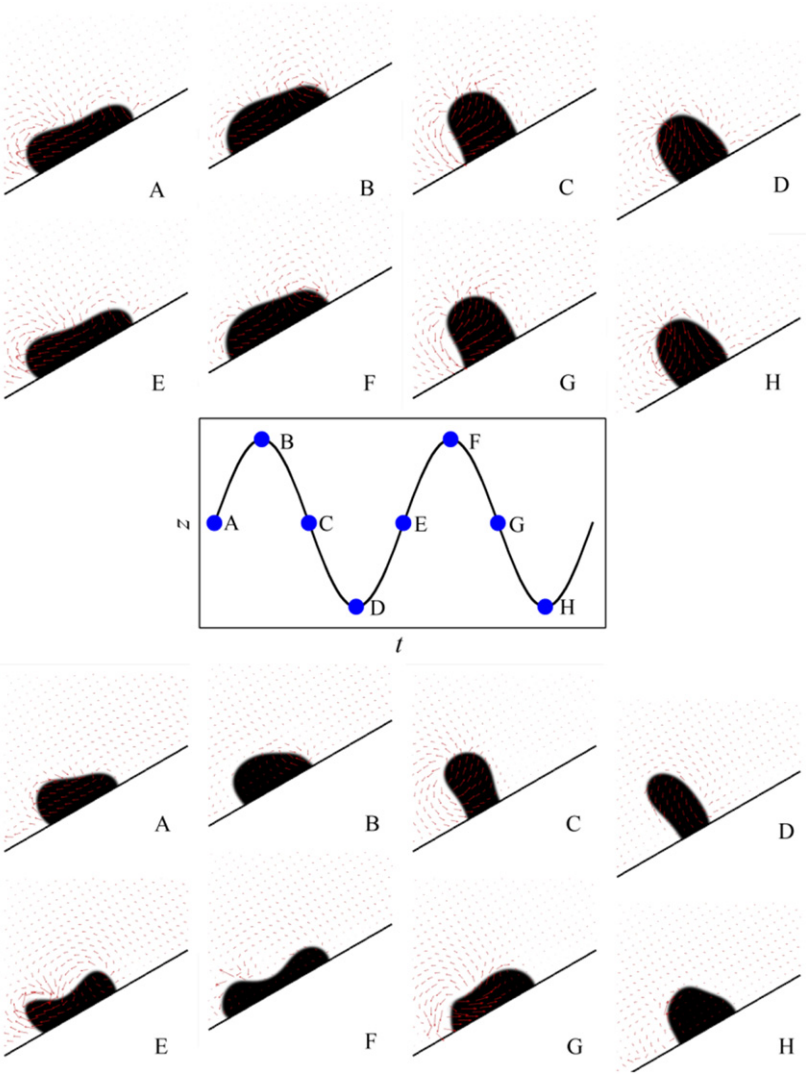

Figure 8. Snapshots of a sliding (top) and climbing (bottom) 2D water drop taken at different instants of a vibrating cycle as indicated in the middle panel. The sliding drop corresponds to the case with $a/a_0 = 1$ and $f/f_0 = 1.33$, while the climbing drop to $a/a_0 = 1.9$ and $f/f_0 = 1.67$. The arrows represent the calculated velocity in both fluids.

The drop shape and the velocity field at different instants of the plate oscillating period are shown in figure 8 during both sliding and climbing. In agreement with the experiments, during sliding the drop undergoes smaller deformations: the border is more rounded and the maximum horizontal and vertical elongations are smaller. Furthermore the periodicity of the sliding drop is the same as that of the plate. Instead, the climbing drop shows a sub-harmonic response with twice the periodicity of the oscillating plate, which does not seem to be confirmed by the experiments and is probably related to the approximations introduced in the model (see supplemental material for a more complete discussion).

The time evolution of the contact line positions and of both upper and lower contact angles can be derived from the analysis of the droplet shape. Figure 9 compares the sliding (left panels) and the climbing (right panels) cases and the double period is again apparent in the upper front of the climbing drop. Full symbols correspond to the lower contact line, empty symbols to the upper contact line. As a reference, the vertical position of the plate is represented by a solid green line. In agreement with the experiments, the simulations of the sliding drop clearly show a phase shift of the contact line motion: when the plate goes up, the drop squeezes down and the lower contact line moves down while the other one goes up. The maximum tangential elongation is reached slightly before the plate reaches its maximum height. Overall, the capillary stresses act like a spring to restore the equilibrium shape. A similar dynamics is observed when the plate descends: the drop retracts and elongates vertically with the lower contact line moving up and the upper one going down. Again, the capillary stresses act against the strong deformation and the motion of the contact lines before the plate reaches its minimum height. The dynamic of the climbing drop is far more complicated as a result of the higher deformation experienced during the plate oscillation (see again the snapshots in figure 8). The phase shift is still present, but in the case

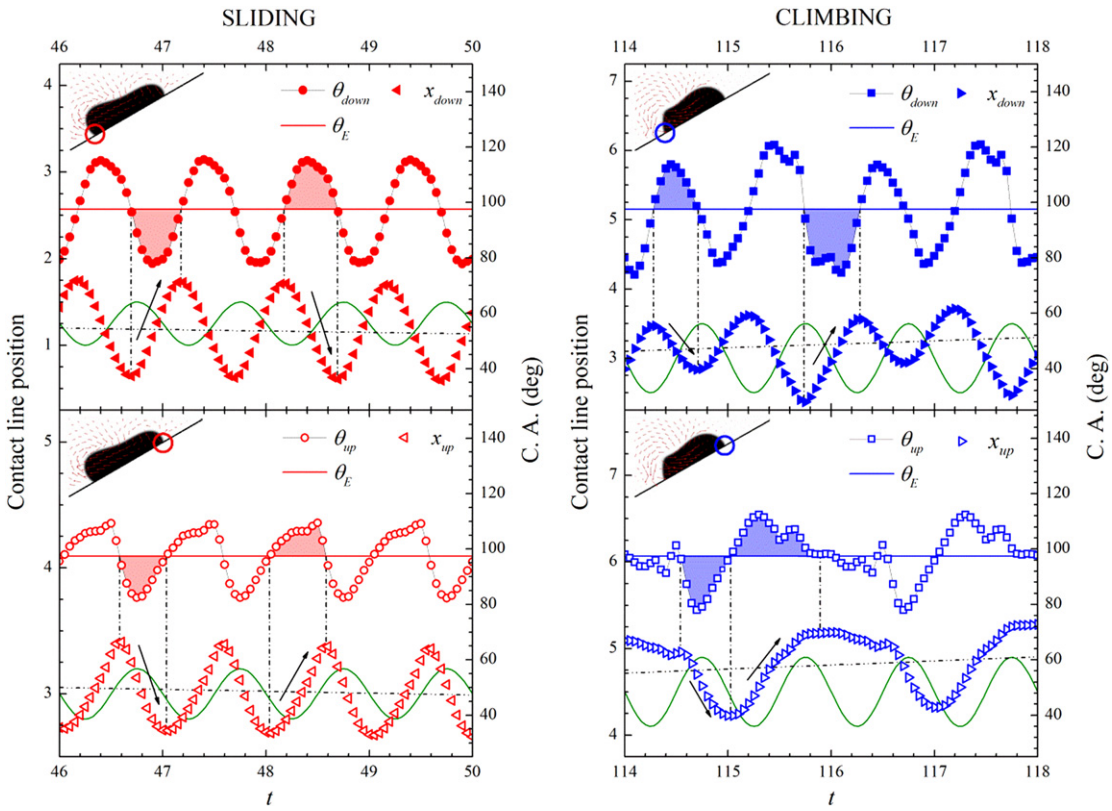

Figure 9. Time evolution of the lower (full symbols) and upper (empty symbols) contact line positions (triangles) and of the contact angles (circles and squares) both in the sliding (left panels) and in the climbing (right panels) regime. The vertical position of the plate is indicated by a sinusoidal green solid line. The contact line position is expressed in unit of the resting drop radius (1 mm) and the time unit is the oscillation period.

shown in figure 9 it is not so pronounced. Moreover, the upper contact line stops sliding down during the plate descent, in a sort of dynamical pinning that enhances the climbing.

Besides the analysis of the drop shape, the numerical simulations provide details about the stress distribution. The momentum equation (4) can be rewritten in conservative form by defining the viscous stress tensors as usual, $\tau^v = (\nabla \boldsymbol{u} + \nabla \boldsymbol{u}^T)/\,\mathrm{Re}$, and recasting the capillary stress in the form of the Korteweg stress, $\tau^c = -\mathrm{Cn}\,(\nabla\Phi \otimes \nabla\Phi)/\mathrm{We}$. By numerical integration of the divergence of the stress tensor $(\tau^v + \tau^c)$ over the entire domain it is possible to extract the total force acting on the fluid. In particular the component in the x direction (parallel to the wall) is

$$\begin{aligned}\int_\Omega \left[\frac{\partial\left(\tau^v{}_{xx_j} + \tau^c{}_{xx_j}\right)}{\partial x_j} + \frac{1}{\mathrm{Fr}} g_x\right] \mathrm{d}V &= \int_{\partial\Omega} \left(\tau^v{}_{xx_j} + \tau^c{}_{xx_j}\right) n_j \mathrm{d}S + W \\ &= \int_{\mathrm{plate}} \left(\tau^v{}_{xx_j} + \tau^c{}_{xx_j}\right) n_j \mathrm{d}S + W \\ &= F_{\mathrm{visc}} + F_{\mathrm{cap}} + W, \end{aligned} \tag{13}$$

where W is the integral of the buoyancy force in the x direction due to the plate vibration and F_{visc} and F_{cap} are the viscous and capillary forces, respectively. The integral over the whole border $\partial\Omega$ reduces to an integral over the plate because of the periodic boundary conditions in the x direction and because we have undisturbed flow conditions and uniform phase field far away from the plate.

Figure 10 shows the time evolution of the viscous and capillary forces during two consecutive plate oscillations. The left panel refers to a sliding drop, the right one to a climbing drop. In both cases the two forces are not in phase with respect to the plate position. The time average of the resulting force equals zero since, on average, the motion is a steady sliding or climbing. The main difference between sliding or climbing is in the sign of the individual forces. In particular, the mean viscous force always acts in the direction of the mean motion.

This result suggests a possible mechanism for droplet motion: following the sketch in figure 11, a downhill-directed viscous force on the drop together with a mean motion in the same direction can be obtained by a circulatory motion of the fluid inside the drop. As a consequence, the drop rolls down. On the contrary, when

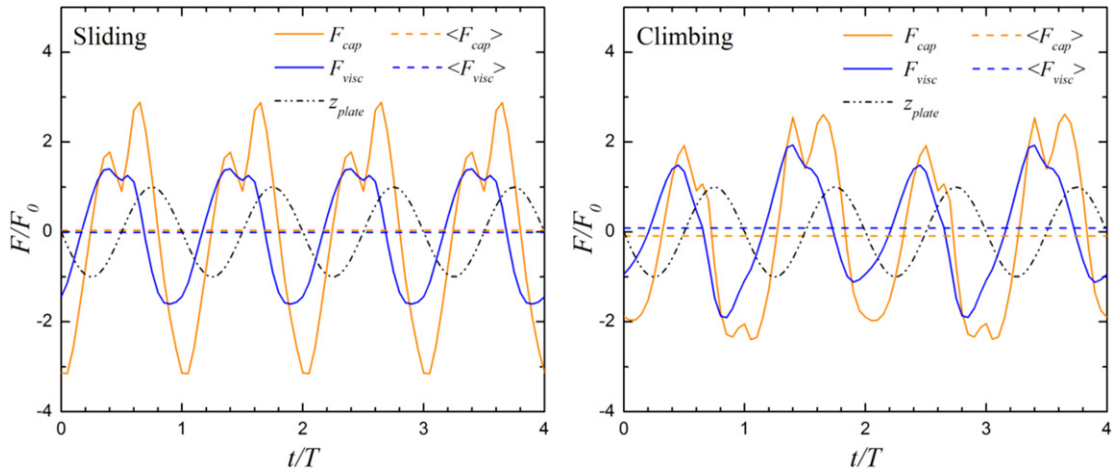

Figure 10. Time evolution of the capillary and viscous forces acting on the drop. T is the period of the plate oscillation and F_0 is a reference force defined as $F_0 = \rho R^3/T^2$, with ρ density of the liquid and R radius of the drop. The left panel represents the sliding case, the right panel the climbing one. The vertical oscillation of the inclined plate z_{plate} is represented in arbitrary unit.

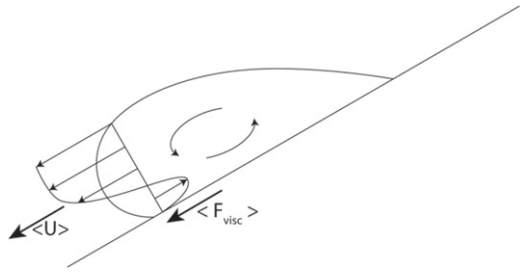

Figure 11. Sketch of the rolling mean motion inside a sliding drop. Both the mean velocity and the mean viscous force are directed downhill.

the drop climbs the plate, the circulatory motion reverts sign (uphill rolling). To be more quantitative, we evaluated the mean circulation in the droplet interface by integrating the mean vorticity:

$$\langle \Gamma \rangle = \frac{1}{2T}\int_{2T}\int_{\partial S} \boldsymbol{u}\cdot \mathrm{d}\ell \mathrm{d}t = \frac{1}{2T}\int_{2T}\int_{S} \nabla \times \boldsymbol{u} \mathrm{d}S\mathrm{d}t, \tag{14}$$

where the drop is identified as the region where $\Phi > 0$. All sliding drops show positive values of $\langle \Gamma \rangle$ while climbing drops have $\langle \Gamma \rangle < 0$, confirming the conjectured rolling motion.

4. Conclusions

In conclusion, we have systematically studied the dynamics of liquid drops on an inclined plate subject to vertical vibrations. The liquids comprised distilled water and different aqueous solutions of glycerol, of ethanol and of isopropanol spanning the range 1–39 $\text{mm}^2\,\text{s}^{-1}$ in kinematic viscosity and 40–72 $\text{mN}\,\text{m}^{-1}$ in surface tension. At sufficiently low oscillating amplitudes, the drops are always pinned to the surface. Vibrating the plate above a certain amplitude yields sliding of the drop. Further increasing the oscillating amplitude drives the drop upward against gravity. The viscosity of the liquid solution does not seem to affect significantly the dynamical phase diagrams, at least in the explored range 1–39 $\text{mm}^2\,\text{s}^{-1}$. Instead, low surface tensions, i.e. low contact angles, are found to hinder climbing and favor sliding of drops. Complementary numerical simulations of 2D drops based on a diffuse interface approach essentially confirm the experimental findings. The overall qualitative behavior is reproduced suggesting that the contact line pinning due to contact angle hysteresis is not necessary to explain the drop climbing. Images taken with a fast camera show that the drop profile evolves in a different way during sliding and climbing as also confirmed by the numerical simulation. The exploitation of these effects offer the possibility to control and manipulate droplets on a substrate by tuning frequency and acceleration of the vertical vibration and drop volume, as shown in Movie3 in supplemental material.

Acknowledgments

We are particularly grateful to Nicola Galvanetto, Davide Stefani and Valdo Chilese for support in the acquisition data. Funding from European Research Council under the European Community's Seventh Framework Programme (FP7/2007-2013)/ERC Grant Agreement N. 297004 is gratefully acknowledged.

References

[1] Rio E, Daerr A, Andreotti B and Limat L 2005 Boundary conditions in the vicinity of a dynamic contact line: experimental investigation of viscous drops sliding down an inclined plane *Phys. Rev. Lett.* **94** 024503
[2] Le Grand N, Daerr A and Limat L 2005 Shape and motion of drops sliding down an inclined plane *J. Fluid Mech.* **541** 293–315
[3] Varagnolo S, Ferraro D, Fantinel P, Pierno M, Mistura G, Amati G, Biferale L and Sbragaglia M 2013 Stick-slip sliding of water drops on chemically heterogeneous surfaces *Phys. Rev. Lett.* **111** 066101
[4] Suzuki S, Nakajima A, Sakai M, Hashimoto A, Yoshida N, Kameshima Y and Okada K 2008 Rolling and slipping motion of a water droplet sandwiched between two parallel plates coated with fluoroalkylsilanes *Appl. Surf. Sci.* **255** 3414–20
[5] Nakajima A, Nakagawa Y, Furuta T, Sakai M, Isobe T and Matsushita S 2013 Sliding of water droplets on smooth hydrophobic silane coatings with regular triangle hydrophilic regions *Langmuir* **29** 9269–75
[6] Varagnolo S, Schiocchet V, Ferraro D, Pierno M, Mistura G, Sbragaglia M, Gupta A and Amati G 2014 Tuning drop motion by chemical patterning of surfaces *Langmuir* **30** 2401–9
[7] Chaudhury M K and Whitesides G M 1992 How to make water run uphill *Science* **256** 1539–41
[8] Savva N and Kalliadasis S 2013 Droplet motion on inclined heterogeneous substrates *J. Fluid Mech.* **725** 462–91
[9] Mugele F and Baret J C 2005 Electrowetting: from basics to applications *J. Phys.: Condens. Matter* **17** R705–74
[10] Yeo L Y and Friend J R 2014 Surface acoustic wave microfluidics *Annu. Rev. Fluid Mech.* **46** 379–406
[11] Quere D 2013 Leidenfrost dynamics *Annu. Rev. Fluid Mech.* **45** 197–215
[12] Daniel S and Chaudhury M K 2002 Rectified motion of liquid drops on gradient surfaces induced by vibration *Langmuir* **18** 3404–7
[13] Dong L, Chaudhury A and Chaudhury M K 2006 Lateral vibration of a water drop and its motion on a vibrating surface *Eur. Phys. J.* E **21** 231–42
[14] Brunet P, Eggers J and Deegan R D 2007 Vibration-induced climbing of drops *Phys. Rev. Lett.* **99** 144501
[15] Brunet P, Eggers J and Deegan R D 2009 Motion of a drop driven by substrate vibrations *Eur. Phys. J.—Spec. Top.* **166** 11–4
[16] Noblin X, Kofman R and Celestini F 2009 Ratchetlike motion of a shaken drop *Phys. Rev. Lett.* **102** 194504
[17] John K and Thiele U 2010 Self-ratcheting stokes drops driven by oblique vibrations *Phys. Rev. Lett.* **104** 107801
[18] Benilov E S and Billingham J 2011 Drops climbing uphill on an oscillating substrate *J. Fluid Mech.* **674** 93–119
[19] Benilov E S 2011 Thin three-dimensional drops on a slowly oscillating substrate *Phys. Rev.* E **84** 066301
[20] Seppecher P 1996 Moving contact lines in the Cahn–Hilliard theory *Int. J. Eng. Sci.* **34** 977–92
[21] Jacqmin D 2000 Contact-line dynamics of a diffuse fluid interface *J. Fluid Mech.* **402** 57–88
[22] Yang X, Feng J J, Liu C and Shen J 2006 Numerical simulations of jet pinching-off and drop formation using an energetic variational phase-field method *J. Comput. Phys.* **218** 417–28
[23] Sui Y, Ding H and Spelt P D M 2014 Numerical simulations of flows with moving contact lines *Annu. Rev. Fluid Mech.* **46** 97–119
[24] Lee J, Son S W, Ha M Y and Kim H R 2014 A numerical study on the dynamic behavior of the liquid located between pillar-shaped structures *J. Mech. Sci. Technol.* **28** 4221–32
[25] Semprebon C and Brinkmann M 2014 On the onset of motion of sliding drops *Soft Matter* **10** 3325–34
[26] Sbragaglia M, Biferale L, Amati G, Varagnolo S, Ferraro D, Mistura G and Pierno M 2014 Sliding drops across alternating hydrophobic and hydrophilic stripes *Phys. Rev.* E **89** 012406
[27] Wang X-P, Qian T and Sheng P 2008 Moving contact line on chemically patterned surfaces *J. Fluid Mech.* **605** 59–78
[28] Dupont J-B and Legendre D 2010 Numerical simulation of static and sliding drop with contact angle hysteresis *J. Comput. Phys.* **229** 2453–78
[29] Toth T, Ferraro D, Chiarello E, Pierno M, Mistura G, Bissacco G and Semprebon C 2011 Suspension of water droplets on individual pillars *Langmuir* **27** 4742–8
[30] Khattab I S, Bandarkar F, Fakhree M A A and Jouyban A 2012 Density, viscosity, and surface tension of water plus ethanol mixtures from 293 to 323 K *Korean J. Chem. Eng.* **29** 812–7
[31] Association G P 1963 *Physical Properties of Glycerine and its Solutions* (New York: Glycerine Producers' Association)
[32] Carlson A, Bellani G and Amberg G 2012 Contact line dissipation in short-time dynamic wetting *Epl* **97** 6
[33] Magaletti F, Picano F, Chinappi M, Marino L and Casciola C M 2013 The sharp-interface limit of the Cahn–Hilliard/Navier–Stokes model for binary fluids *J. Fluid Mech.* **714** 95–126
[34] Celestini F and Kofman R 2006 Vibration of submillimeter-size supported droplets *Phys. Rev.* E **73** 041602
[35] Bonn D, Eggers J, Indekeu J, Meunier J and Rolley E 2009 Wetting and spreading *Rev. Mod. Phys.* **81** 739–805
[36] Winkels K G, Peters I R, Evangelista F, Riepen M, Daerr A, Limat L and Snoeijer J H 2011 Receding contact lines: from sliding drops to immersion lithography *Eur. Phys. J.—Spec. Top.* **192** 195–205